

Prospects for detection of detached double white dwarf binaries with *Gaia*, LSST and LISA

Valeriya Korol,^{1★} Elena M. Rossi,¹ Paul J. Groot,² Gijs Nelemans,^{2,3}
Silvia Toonen^{1,4} and Anthony G. A. Brown¹

¹*Leiden Observatory, Leiden University, PO Box 9513, NL-2300 RA Leiden, the Netherlands*

²*Department of Astrophysics, IMAPP, Radboud University, PO Box 9010, NL-6500 GL Nijmegen, the Netherlands*

³*Institute for Astronomy, KU Leuven, Celestijnenlaan 200D, B-3001 Leuven, Belgium*

⁴*Astronomical Institute Anton Pannekoek, University of Amsterdam, PO Box 94249, NL-1090 GE Amsterdam, the Netherlands*

Accepted 2017 May 22. Received 2017 May 22; in original form 2017 March 1

ABSTRACT

Double white dwarf (DWD) binaries are expected to be very common in the Milky Way, but their intrinsic faintness challenges the detection of these systems. Currently, only a few tens of *detached* DWDs are known. Such systems offer the best chance of extracting the physical properties that would allow us to address a wealth of outstanding questions ranging from the nature of white dwarfs and thermonuclear supernovae, over stellar and binary evolution to mapping the Galaxy. In this paper, we explore the prospects for detections of ultra-compact (with binary separations of a few solar radii or less) detached DWDs in (1) optical radiation with *Gaia* and the Large Synoptic Survey Telescope (LSST) and (2) gravitational wave radiation with Large Synoptic Survey Telescope (LISA). We show that *Gaia*, LSST and LISA have the potential to detect, respectively, around a few hundred, a thousand and 25 thousand DWD systems. Moreover, *Gaia* and LSST data will extend by, respectively, a factor of 2 and 7 the guaranteed sample of LISA verification sources, binaries detectable in electromagnetic and gravitational wave radiation, opening the era of multimessenger astronomy for these sources.

Key words: gravitational waves – binaries: close – binaries: eclipsing – white dwarfs.

1 INTRODUCTION

On the basis of our theoretical understanding of stellar and binary evolution, systems of two white dwarfs in a close binary were predicted since 1980s (thereafter double white dwarf (DWD) binaries) (Tutukov & Yungelson 1981; Iben & Tutukov 1984b; Webbink 1984; Tutukov & Yungelson 1988; Iben, Tutukov & Yungelson 1997; Han 1998; Nelemans et al. 2000, 2001a; Toonen, Nelemans & Portegies Zwart 2012). However, due to their intrinsic faintness, the first detection came only a decade later in 1988 (Saffer, Liebert & Olszewski 1988). The current census counts a few tens of DWDs discovered by spectroscopic and variability surveys such as the SPY (ESO SN Ia Progenitor) survey (e.g. Napiwotzki et al. 2003), the ELM (Extremely Low Mass WDs) survey (e.g. Brown et al. 2010) and studies by Marsh (1995), Marsh, Dhillion & Duck (1995), Maxted & Marsh (1999) and Badenes et al. (2009). Still, these represent only a fraction of the DWD binaries predicted in numerical simulations (Toonen et al. 2017).

Substantial progress in the detection of these sources is expected with optical wide surveys such as *Gaia* (Gaia Collabora-

tion et al. 2016) and the Large Synoptic Survey Telescope (LSST) (LSST Science Collaboration et al. 2009), and in gravitational waves (GWs) with the Laser Interferometer Space Antenna (LISA) mission (Amaro-Seoane et al. 2012). All three instruments will be sensitive to short period ($P < \text{a few days}$) binaries (e.g. Prša, Pepper & Stassun 2011; Eyser et al. 2012; Nelemans 2013; Carrasco et al. 2014) and will provide a large sample of new ultra-compact DWDs that are interesting for several reasons. First, compact DWDs are systems that experienced at least two phases of mass transfer and thus provide a good test for binary evolution models, and, in particular, for our understanding of mass transfer and the common envelope (CE) phase. Secondly, DWDs are the plausible progenitors to a wide range of interesting systems: Type Ia supernovae (Iben & Tutukov 1984a; Webbink 1984) that are used as cosmological distance indicators (e.g. Riess et al. 1998; Perlmutter et al. 1999), AM CVn systems (Nelemans et al. 2001a; Marsh, Nelemans & Steeghs 2004; Solheim 2010) and ‘fast optical transients’ including Ia supernovae, Ca-rich transients and fast/bright transients (Bildsten et al. 2007; Perets et al. 2010; García-Berro et al. 2017). In addition, it is believed that the merger of two WDs can produce rare stars such as massive WDs (or even an isolated neutron star), subdwarf-O and R Corona Borealis stars (Webbink 1984; Longland et al. 2011). Thirdly, DWDs represent guaranteed sources for

★ E-mail: korol@strw.leidenuniv.nl

Table 1. Distribution of the initial binary parameters.

Parameter	Distribution	Range of definition
Mass of stars	Kroupa IMF ^a	$0.95 < M M_{\odot} < 10$
Binary mass ratio	Uniform in q^b	$0 < q \leq 1$
Orbital separation	Uniform in $\log a^c$	$0 \leq \log \frac{a}{R_{\odot}} \leq 6$
Eccentricity	Thermal ^d	$0 \leq e \leq 1$
Inclination	Uniform in $\cos i$	$0 \leq \cos i \leq 1$

References: ^aKroupa, Tout & Gilmore (1993);^bDuchêne & Kraus (2013);^cAbt (1983);^dHeggie (1975);

the LISA mission and will dominate the low-frequency gravitational waveband from mHz to a few Hz (e.g. Evans, Iben & Smarr 1987; Lipunov & Postnov 1987; Hils, Bender & Webbink 1990; Nelemans, Yungelson & Portegies Zwart 2001b; Lorén-Aguilar et al. 2005; Ruiter et al. 2010; Marsh 2011; van den Broek et al. 2012). Finally, detached DWD binaries with orbital periods in the range from 1-h to a few minutes are particularly suitable for studying the physics of tides, a phenomenon directly related to the WD internal properties. The study of the reaction of the stellar internal structure to tidal forces may give us important information, for example, on the WD viscosity and its origin, that will complete our knowledge on the WD interior matter (Piro 2011; Fuller & Lai 2012; Dall’Osso & Rossi 2014; McKernan & Ford 2016).

In this paper, we compute the size of a sample of Galactic ultra-compact detached DWD binaries that could be observed with future facilities in the next two decades. In particular, we predict the size (likewise Cooray, Farmer & Seto 2004; Littenberg et al. 2013; Shah, Nelemans & van der Sluis 2013) and properties of the sample that will be observed in both electromagnetic (EM) and GW radiation by *Gaia*, LSST and LISA: despite the widespread expectation that those instruments will represent major step forward, quantitative predictions have never been published. We characterize the physical properties of these samples and compare them to current data.

The paper is organized as follows. In Section 2, we will describe the method we use to simulate the Galactic population of DWDs. In Section 3, we will estimate how many binaries can be detected with *Gaia* and LSST as eclipsing sources. In Section 4, we will focus on the GW emission from these sources and we assess the prospects for detections by the upcoming LISA mission. In Section 5, we will present and characterize the sample of DWDs detectable through EM and GW radiation. Finally, we will discuss our results and possible synergies between GW and EM observations.

2 SIMULATED DWD POPULATION

To obtain a model sample of the Galactic DWD population, we use the binary population synthesis code *SEBA*, developed by Portegies Zwart & Verbunt (1996, for updates see Nelemans et al. 2001a, Toonen et al. 2012). The initial stellar population is obtained from a Monte Carlo-based approach, assuming a binary fraction of 50 per cent and distributions of the initial binary parameters in Table 1. In particular, we draw the mass of single stars from the Kroupa initial mass function (IMF; Kroupa et al. 1993). The mass of the secondary star is drawn from a flat mass ratio distribution. This is a poorly constrained relationship that, in general, depends on the stellar population. A typical progenitor of a DWD component is an A-type star (De Rosa et al. 2014). For this stellar type, a

flat mass ratio distribution is a good first-order approximation when comparing to observations (Duchêne & Kraus 2013). The orbit eccentricity is drawn from a thermal distribution expected from an energy equipartition argument and often recovered from observations (Heggie 1975; Raghavan et al. 2010). Besides, DWDs lose the memory of the initial orbital eccentricity because they circularize at quite early stages of their evolution, thus the shape of the initial eccentricity distribution hardly influences our simulation. The most common assumptions for the binary orbital period (or semimajor axis) distribution are logarithmically flat and lognormal. For intermediate-mass and solar-mass stars, both are consistent with observations (e.g. Poveda, Allen & Hernández-Alcántara 2007; Raghavan et al. 2010; Duchêne & Kraus 2013; Tokovinin, Mason & Hartkopf 2014). The largest differences between the two are expected for both very short or for very long period systems, but such systems are not likely to be progenitors of a typical DWD. Moreover, Toonen et al. (2017, see tables 4 and 5) do not find significantly different numbers of DWDs when performing simulations (analogous to ours) with both logarithmically flat and lognormal distributions. Therefore, in our simulation, we adopt a logarithmically flat distribution. Finally, for each binary we assign an inclination angle i , drawn from the uniform distribution in $\cos i$. We explore the sensitivity of these assumptions by performing simulations for different choice of the IMF and mass ratio relation. We discuss the impact of our assumptions in Section 6.

To take into account the star formation history of the Galaxy, we exploit a code originally developed by Nelemans et al. (2001a), Nelemans, Yungelson & Portegies Zwart (2004) and updated by Toonen & Nelemans (2013). The code distributes binaries according to a Galactic model with two components: disc and bulge. The density of DWDs in the disc is given by

$$P(R, t, z) = \rho_{BP}(R, t) \text{sech}^2\left(\frac{z}{z_h}\right) \text{pc}^{-3}, \quad (1)$$

where $0 \leq R \leq 19$ kpc is the cylindrical radius from the Galactic Centre, ρ_{BP} is the result of the integration in R and t of the plane-projected star formation rate (SFR) from Boissier & Prantzos (1999), z is height above the disc, $z_h = 300$ pc is the disc scaleheight and the age of the Galaxy is assumed to be 13.5 Gyr (Jurić et al. 2008; Binney & Tremaine 2011). We neglect the dependence on the stellar age and mass when assigning z , and we assume that there is no radial migration of the stars in time. We model the Galactic bulge by doubling the SFR in the inner 3 kpc of the Galaxy and distributing sources spherically:

$$\rho_{bulge}(r) \propto e^{(r/r_b)^2} \text{pc}^{-3}, \quad (2)$$

where r is the spherical distance from the Galactic Centre and $r_b = 0.5$ kpc is the characteristic radius of the bulge (Sofue, Honma & Omodaka 2009; Binney & Tremaine 2011). We normalize equation (2) such that the total mass of the bulge at $t = 13.5$ Gyr is $2.6 \times 10^{10} M_{\odot}$. The resulting distribution of DWDs at different Galactic ages is represented in Fig. 1. To show the portion of the Galaxy that can be potentially observed by *Gaia* and LSST, we colour in magenta and blue stars, respectively, with apparent magnitudes <20 and <24 .

The absolute magnitudes for WDs are deduced from the WD cooling curves of pure hydrogen atmosphere models (Holberg & Bergeron 2006; Kowalski & Saumon 2006; Tremblay, Bergeron & Gianninas 2011, and references therein¹). To convert the absolute

¹ See also <http://www.astro.umontreal.ca/~bergeron/CoolingModels>

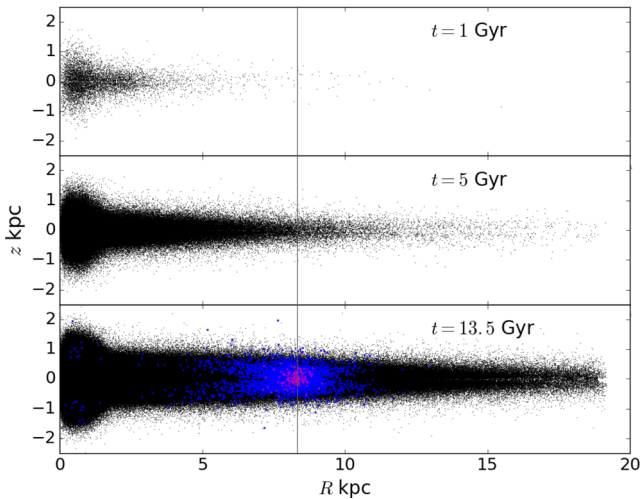


Figure 1. The distribution of DWDs in the Galaxy at $t = 1, 5$ and 13.5 Gyr. R is the cylindrical radius from the Galactic centre and z is the height above the Galactic disc. The grey vertical line marks the position of Sun. We represent in magenta and blue, respectively, DWDs potentially accessible to *Gaia* and to LSST.

magnitudes to observed magnitudes (e.g. for the Sloan r band), we use the following expression:

$$r_{\text{obs}} = r_{\text{abs}} + 10 + 5 \log d + 0.84 A_V, \quad (3)$$

where d is the distance to the source in kpc, $0.84 A_V$ is the extinction in the Sloan r band, obtained from the extinction in the V band, A_V . To compute the value of A_V at the source position, defined by the Galactic coordinates (l, b) at the distance d , we use

$$A_V(l, b, d) = A_V(l, b) \tanh \left(\frac{d \sin b}{h_{\text{max}}} \right), \quad (4)$$

where $A_V(l, b)$ is the integrated extinction in the direction defined by (l, b) from Schlegel, Finkbeiner & Davis (1998), $h_{\text{max}} \equiv \min(h, 23.5 \times \sin b)$ and $h = 120$ pc is the Galactic scaleheight of the dust (Jonker et al. 2011). To convert r magnitudes into *Gaia* G magnitude, we applied a colour–colour polynomial transformation with coefficients according to Carrasco et al. (2014, table 6). Finally, for our simulation, we apply a magnitude limit of $r = 70$ and a period limit of $P = 20$ d. The magnitude limit is chosen to ensure that the simulated population can also be used for the GW detection simulations.

There are at least two phases of mass transfer in the standard picture of formation of a DWD system. To form a short-period DWD binary, at least one mass transfer phase needs to be a CE (Paczynski 1976; Webbink 1984). In our simulation, we adopt two evolutionary scenarios, with two different treatments of the CE phase: the $\alpha\alpha$ and the $\gamma\alpha$ scenarios. In the $\alpha\alpha$ scenario, the CE phase is described by the so-called α -formalism (see Ivanova et al. 2013, for review). In this prescription, the CE outcome is determined by the conservation of the orbital energy (Webbink 1984), where α represents the efficiency in the exchange of the orbital energy and the binding energy of the envelope, described by another free parameter of the model λ . The two parameters can be combined using equations (2) and (3) of Toonen & Nelemans (2013) to a single unknown $\alpha\lambda$. Based on Nelemans et al. (2000), we adopt to be $\alpha\lambda = 2$. In the second scenario, proposed in order to explain properties of observed DWDs, the CE is described by an alternative γ parametrization (Nelemans et al. 2000; Nelemans & Tout 2005). In the γ -formalism, the binary orbital evolution is driven by angular

momentum loss that is carried away through the mass-loss process, and γ is the efficiency of this mechanism. In the $\gamma\alpha$ prescription, the γ -formalism is applied whenever a binary does not contain a compact object or when the CE is not driven by a tidal instability, in which case, the α prescription is used. Thus, in the $\gamma\alpha$ scenario, the first CE is typically described by the γ formalism and the second by the α formalism. For this scenario, we assume the value of the $\alpha\lambda$ as in the $\alpha\alpha$ CE model and $\gamma = 1.75$ (Nelemans et al. 2000).

The main differences between the two populations obtained with these different prescriptions are the total number of binaries and their mass ratio distribution. Using the $\gamma\alpha$ model, one typically obtains twice as many binaries compared to the $\alpha\alpha$ scenario. Moreover, the mass ratio distribution in the $\gamma\alpha$ spans a wider range of values, which agrees better with the currently observed DWD population, while the majority of the population formed via $\alpha\alpha$ scenario will show mass ratios around 0.5 (see Toonen et al. 2012, fig. 2). This is due to the fact that in the α prescription, the orbit always shrinks significantly. When using the γ prescription, the CE outcome heavily depends on the binary mass ratio (see e.g. equation A16 of Nelemans et al. 2001a): for a roughly equal mass binary, the orbit does not change much, however, for a binary with very different mass components, the orbit shrinks strongly.

3 EM DETECTION

In this section, we focus our analysis on two instruments: *Gaia* and the LSST. Being photometric variability surveys, both are expected to mostly detect new DWDs through eclipses (Eyer et al. 2012) and thus selecting mainly short-period ones. These DWDs are the most interesting for studying the final stages of binary evolution and represent potential GW sources.

Gaia is a space mission, launched on 2013 December 19, whose primary goal is to provide a detailed 3D distribution and space motion of a billion stars in our Galaxy (Gaia Collaboration et al. 2016). During 5 yr of mission, *Gaia* will deliver positions, parallaxes and proper motions for all stars down to $G \simeq 20$ over the whole sky. According to the GUMS (Gaia Universe Model Snapshot) simulation, *Gaia* will see between 250 000 and 500 000 WDs, and more than 60 per cent of them will be in binaries (Carrasco et al. 2014). Astrometrical and multicolour photometrical observations will be possible for the Galactic WD population. The majority of the Galactic WD population is too faint for the radial velocity spectrometer (RVS) onboard of the *Gaia* satellite, and even the brightest ones ($G < 15$) are typically featureless in RVS wavelength range. Thus, no radial velocities will be available for these sources, so to fully characterize them ground-based spectroscopic followup will be necessary (Carrasco et al. 2014; Gaensicke et al. 2015).

The LSST is a ground-based telescope, currently under construction and expected to be fully operational in 2022 (LSST Science Collaboration et al. 2009). It will complement the *Gaia* study of the Milky Way stellar population down to magnitude $r \simeq 24$, with a possibility to extend this photometric limit down to $r \simeq 27$ with image-stacking techniques. The LSST will detect about 10 billion stars up to distances of ~ 100 kpc over half of the sky. In particular, it will allow the discovery of several millions of WDs (LSST Science Collaboration et al. 2009, chapter 6).

The technical characteristics of the two instruments used for our study (sky coverage, average cadence, limiting magnitude and visibility constraints of the survey, etc.) are summarized in Table 2.

Table 2. *Gaia* and the LSST technical characteristics. The quoted parameters are from *Gaia* Collaboration et al. (2016) and LSST Science Collaboration et al. (2009).

	<i>Gaia</i>	LSST
Sky coverage	Whole sky	~1/2 sky
Wavelength coverage	330–1050 nm	<i>ugrizy</i>
Bright limit	–	$r \simeq 16\text{--}17$
Depth per observation	$G \simeq 20.7$	$r \simeq 24$
Syst. photometric error (mag)	0.001	0.005
Integration time (s)	40.5	15 + 15
Nominal mission lifetime	5 yr	10 yr
Average number of observations	70	10^3
Average cadence of observations	1 in 26 d	1 in 3 d

3.1 Simulations of light curves

Next, we simulate the light curves of the obtained DWD model population by using a purely geometrical model. We compute the flux of a binary for given binary parameters: a , R_1 , R_2 , r_1 , r_2 and d , where a is the binary orbital separation, R_1 and R_2 are the respective radii of the two binary components and r_1 and r_2 are their r -band magnitude. Note that in this work, we adopt the definition of the primary as the brightest WD, and secondary as the dimmest WD of the pair.

In this simple treatment, the limb darkening effect is neglected, so stars are considered spherically symmetric with a uniform surface brightness distribution. Gravitational distortion (ellipsoidal variation) and mutual heating are also not taken into account. Neglecting these effects implies looking for photometric variability caused by eclipses alone that limits our search to systems with a very narrow range of inclination angles $i \sim 90^\circ$. For DWDs, the variation in the light curve induced by mutual heating is not expected to be significant, given the small size of WD stars and roughly equal size of binary components. We estimate the maximum flux variation due to the mutual heating to be at most of the same order of magnitude as the average eclipse depth, if we assume the maximum efficiency for this process. To test whether including the ellipsoidal variation in our simulation could enlarge the sample of detectable sources, we estimate how many systems in our simulated population would show the maximum amplitude of the ellipsoidal variation greater than 1 per cent using the theoretical prediction from Hermes et al. (2012):

$$\frac{L(\phi)}{L} = \frac{-3(15 + u_1)(1 + \tau_1)(R_1/a)^3(m_2/m_1)\sin^2 i}{20(3 - u_1)} \cos(2\phi), \quad (5)$$

where L is the total luminosity of the system, $u_1 = 0.1\text{--}0.5$ and $\tau_1 = 1.0$ are the limb-darkening and gravity-darkening coefficients for the primary and $\cos(2\phi) = 1$. We find ~ 20 systems with $G/r < 24$ (in both formation scenarios) with the maximum amplitude of ellipsoidal variation greater than 1 per cent in our simulation. These are the closest and the lightest binaries in our synthetic population as expected from theoretical predictions (e.g. Iben, Tutukov & Fedorova 1998). Thus, including ellipsoidal variation in our simulation would increase the number of detected system by at most a couple of tens of systems.

To evaluate the relative photometric error per single *Gaia* observation, we use

$$\sigma_G = 1.2 \times 10^{-3} (0.04895z^2 + 1.8633z + 0.00001985)^{1/2}, \quad (6)$$

where $z = \max[10^{0.4(12-15)}, 10^{0.4(G-15)}]$ (*Gaia* Collaboration et al. 2016, section 8.2). To evaluate the expected photometric error per single observation with the LSST, we use

$$\sigma_r = (\sigma_{\text{sys}}^2 + \sigma_{\text{rand}}^2)^{1/2}, \quad (7)$$

where, according to LSST Science Collaboration et al. (2009, section 3.5), $\sigma_{\text{sys}} = 0.005$ is the systematic photometric error, $\sigma_{\text{rand}}^2 = (0.04 - \tilde{y})x + \tilde{y}x^2$, $x = 10^{(m-m_5)}$ is the random photometric error, m_5 and \tilde{y} are the 5σ limiting magnitude for a given filter and the sky brightness in a given band, respectively. Finally, we add a Gaussian white noise to our synthetic light curves.

The motion of the *Gaia* satellite is quite complex and cannot be expressed by an analytical formula: it is given by a combination of rotation of the satellite on its own axis, precession of the spin axis itself and the revolution around Sun (Eyer & Mignard 2005). Therefore, to get a realistic light curve sampling with *Gaia*, we used the *Gaia Observation Forecast Tool*² that provides a list of observing times (TCB) per target for a given period of observation and target position on the sky. To get a set of *Gaia* pointings for each binary in our simulation, we use the largest available time interval that spans from 2014-09-26T00:00:00 TCB to 2019-06-01T00:00:00 TCB (~ 5 yr mission lifetime). To simulate the light curve sampling with the LSST, we use the anticipated regular cadence of 3 d over a nominal 10-yr life span of the mission. In Fig. 2, we show a comparison of the light-curve sampling by *Gaia* (top panel) and LSST (bottom panel) for two binaries with similar orbital periods (21 min and 24 min).

In order to count detections, we applied the following criteria. First, we check if the source presents variability by evaluating the χ^2 value of the light curve with respect to the average source magnitude. To establish a χ^2 threshold value above which we consider a source as variable, we compute the χ^2 distribution of non-variable Galactic objects in the *Gaia* magnitude range. The result is represented in Fig. 3. This simple test allows us to distinguish between variability due to a binary nature of the source and variability induced by photometric fluctuations of observations of non-variable objects. In this simulation, we do not take into account any other type of variable stars present in the Galaxy such as pulsating WDs (DAVs: ZZ Ceti), Delta Scuti and SX Phoenicis stars, or variability due to deformation or heating in these binaries (see e.g. Macfarlane et al. 2015; Toma et al. 2016). In real data, these stars will exhibit a similar behaviour to eclipsing DWDs and will contaminate the sample of candidate DWDs. Thus, in general, additional analysis techniques will be required in order to confirm DWD candidates. For the *Gaia* data, this analysis will be done by the *Gaia* Data Processing and Analysis Consortium (Eyer et al. 2014).

It is evident from Fig. 3 that for $\chi^2 > 2$, there is little overlap between the population of non-variable sources (red histogram) and the population of eclipsing binaries. To be conservative, we adopt a threshold value of $\chi^2 = 3$. Finally, we require that a minimum number of data points, N_{samp} , with flux at least 3σ below the out-of-eclipse level, falls within the eclipse phase: for *Gaia*, we adopt $N_{\text{samp}} \geq 3$ and for the LSST $N_{\text{samp}} \geq 10$. This requirement introduces a constrain on the ratio between the duration of the eclipse phase t_{ecl} and the binary orbital period P , such that $t_{\text{ecl}}/P = N_{\text{samp}}/N_{\text{tot}}$, where N_{tot} is the total number of observations per source (see Table 2). By using a geometrical argument, t_{ecl} can be estimated as the time it takes the occulting star to move twice the distance from the first

² <http://gaia.esac.esa.int/gost/>

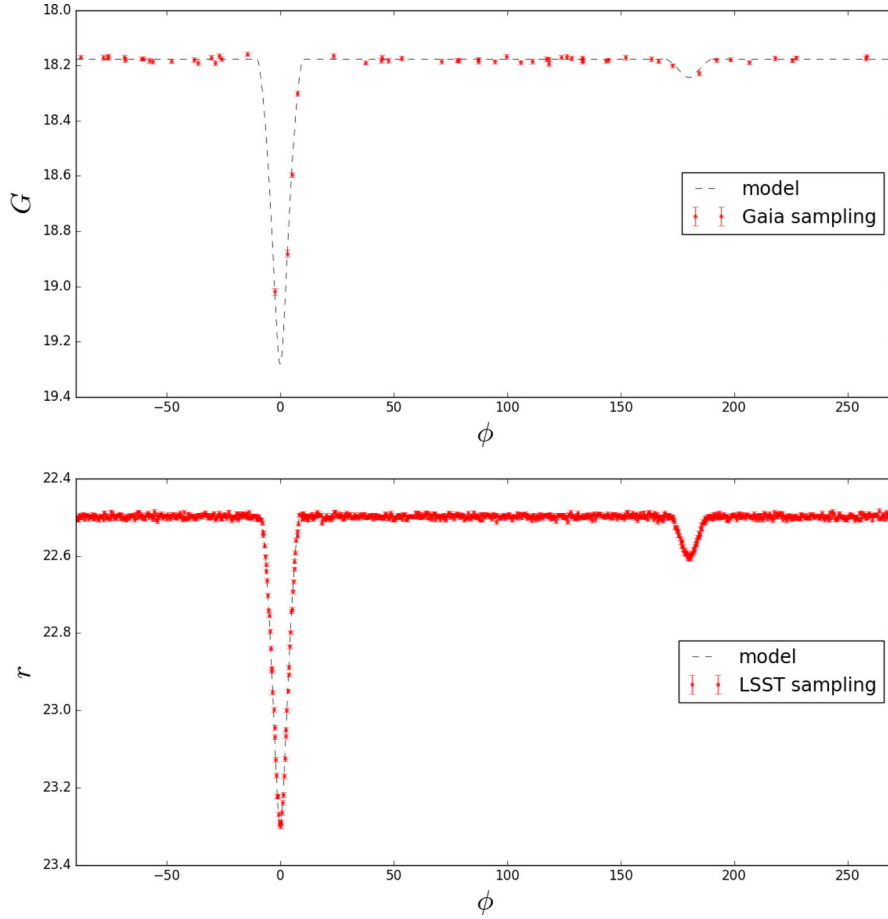


Figure 2. An example of phase-folded light curves sampled with *Gaia* (top panel) and LSST (bottom panel) observations. The periods of the two sources are $P \simeq 21$ min and $P \simeq 24$ min, respectively.

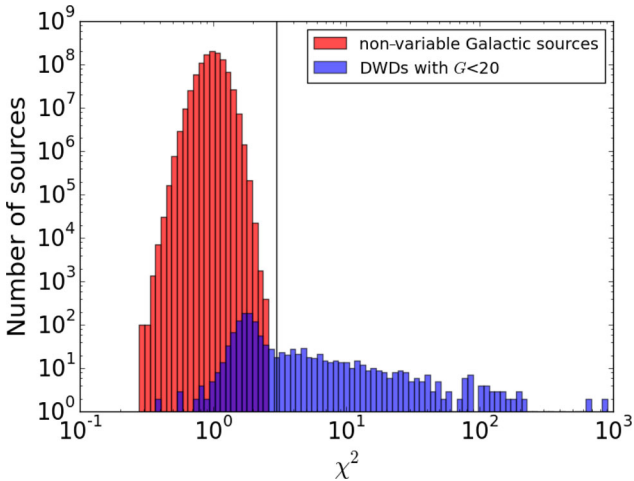


Figure 3. The χ^2 distribution of simulated non-variable Galactic objects (in red) obtained using the classic apparent magnitude (G) distribution expected from star-counts (Prob. $\propto 10^{\gamma G}$, where $0.2 \leq \gamma \leq 0.4$), and the χ^2 distribution of simulated DWDs in *Gaia* visibility range (in blue). The vertical line represents the threshold value $\chi^2 = 3$, above which we claim a detection.

contact (the point when the apparent stellar discs are externally tangent) to mid-eclipse (when stellar centres are aligned), so t_{ecl}/P can be found as

$$\frac{t_{\text{ecl}}}{P} = \frac{\delta}{2\pi a}, \quad (8)$$

where $\delta = 2\sqrt{(R_1 + R_2)^2 - a^2 \cos^2 i}$ and $2\pi a$ is the total length of the orbit. Note that for an edge-on binary $\delta = 2(R_1 + R_2)$. From equation (8), we find that the typical t_{ecl} for a DWD binary in our simulated population is around 2 min. Thus, we expect that *Gaia* will detect systems with typical periods $P \lesssim (t_{\text{ecl}} N_{\text{tot}})/N_{\text{samp}} \lesssim 45$ min. Following a similar reasoning, one can anticipate that LSST will detect eclipsing binaries with $P \lesssim 3$ h.

3.2 Detection efficiency

To assess the detection efficiency of the two instruments, we simulate the sampling of a test light curve by varying the magnitude and period of a binary system with $m_1 = 0.53 M_{\odot}$, $m_2 = 0.35 M_{\odot}$, $R_2 = 0.017 R_{\odot}$, $R_1 = 0.8 R_2$, $d = 1$ kpc and $i = \pi/2$. The chosen parameters for the test light curve represent the average values in our simulated population. For each period P in the range between 5 min and 10 h (with 10 min steps) and magnitude (r or G) between 15 and the photometric limit of the instrument (with 0.25 mag steps), we calculate 100 realizations of the test light-curve sampling by randomly assigning the initial orbital phase. We determine whether the light curve was detected based on the criteria described in

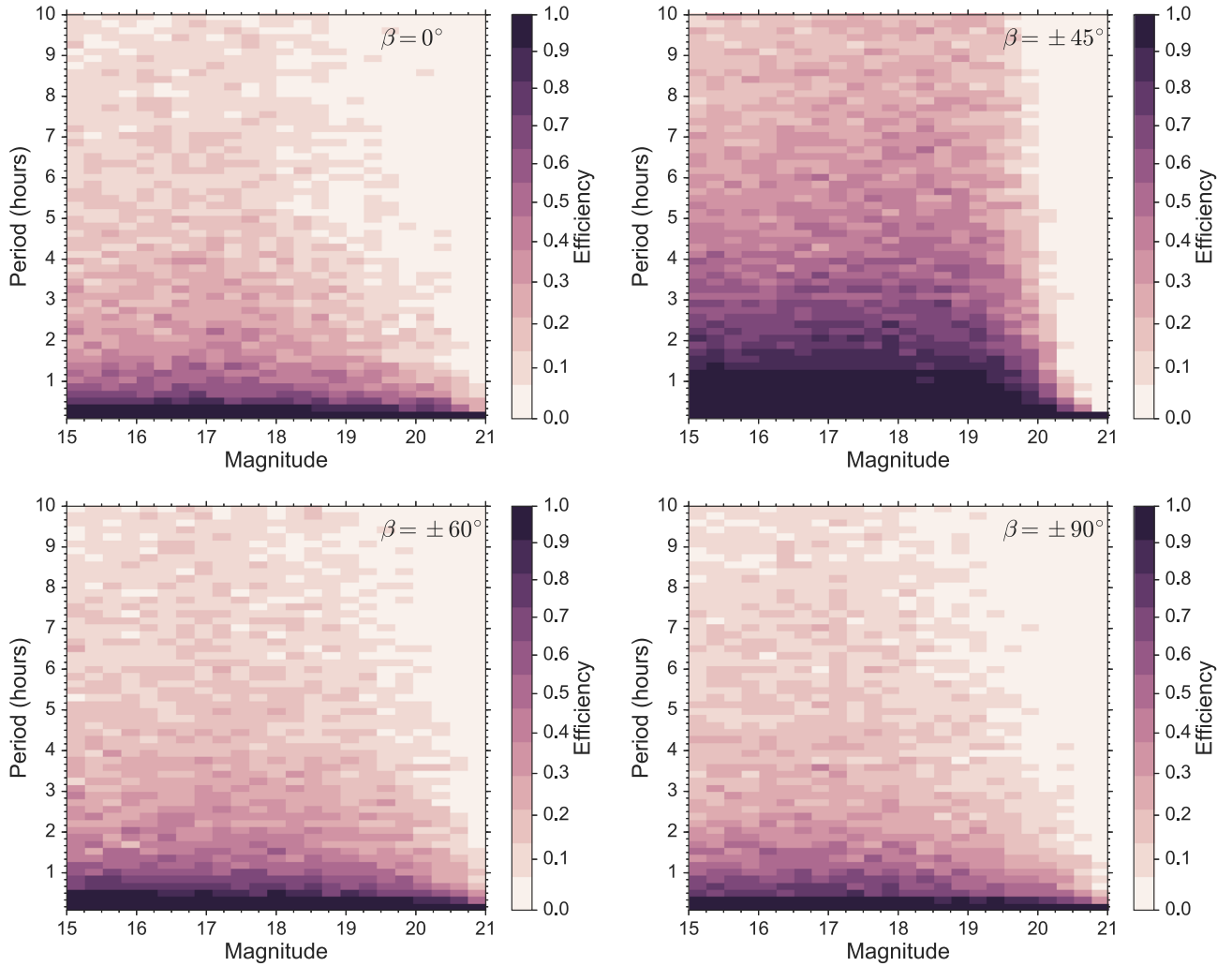


Figure 4. Detection efficiency of *Gaia* at $\beta = 0, +45, +60$ and 90° ecliptic latitudes that corresponds, respectively, to 60, 200, 80 and 70 observations, computed for test binary system with $m_1 = 0.53 M_\odot$, $m_2 = 0.35 M_\odot$, $R_2 = 0.017 R_\odot$, $R_1 = 0.8R_2$, $d = 1$ kpc and $i = \pi/2$. The time step is 10 min and the magnitude step is 0.25. The colour indicates the instrument efficiency from 0 to 1.

Section 3.1. Finally, we represent the detection probability per bin as the number of times the test light curve was detected over 100 realizations.

As discussed in Section 3.1, our detection test depends on the total number of observations per source N_{tot} . For *Gaia*, N_{tot} is uniform in ecliptic longitude λ and has a strong dependence on ecliptic latitude β :³ N_{tot} is minimum at $\beta \sim 0^\circ$, increases up to ~ 200 observations per source at $\beta \pm 45^\circ$ and decreases down to ~ 70 at ecliptic poles $\beta \pm 90^\circ$ (Eyer & Mignard 2005). *Gaia* detection efficiency for $\beta = 0, +45, +60$ and 90° ecliptic latitudes is represented in Fig. 4, where the impact of the different number of observations is evident. Fig. 4 shows that for any fixed period (when the distance to the source is also fixed), *Gaia* generally detects more efficiently brighter binaries, simply because of the photometric performance of the instrument. For example, in the top left panel of Fig. 4, for periods between 2 and 3 h, one can see that the efficiency drops from 0.4–0.3 to 0 for increasing magnitudes. However, for very short periods ($P \lesssim 20$ min), the efficiency remains approximately constant even at the faint end of the *Gaia* visibility range, independent of the number

of observations. At a fixed magnitude, *Gaia* cadence works better for detection of short-period sources: for $G = 18$, the efficiency is >0.4 for $P < 4$ h and >0.9 for $P < 30$ min (Fig. 4, top left panel). This is a consequence of the fact that the eclipse duration is set by the geometry of the system, so the time that the system spends in eclipse compared to the total orbital period is longer for systems with shorter periods (i.e. t_{ecl}/P decreases along the y-axis). Thus, it is more likely to catch the binary in eclipse phase when the period of the binary is shorter. By using this simple argument and assuming a regular cadence of 70 observations, one can preliminarily estimate the average number of detections by counting the number of DWDs in our synthetic population that satisfy $t_{\text{ecl}}/P \geq 3/70$. This gives around 250 DWD systems with $G < 20.7$.

The efficiency of the LSST is illustrated in Fig. 5. For the LSST, we find that the average cadence of one observation in 3 d and the high number of data points make it very efficient at all magnitudes for all orbital periods $\lesssim 10$ h. Drops in efficiency visible in Fig. 5 (e.g. a horizontal stripe at 6 h) corresponds to periods that are submultiples of 72 h, the cadence of observations. As for *Gaia*, we estimate the number of binaries in our simulated population that can be positively detected with at least 10 observation per eclipse. We find around $\sim 1.9 \times 10^3$ binaries with $r < 24$.

³ <https://www.cosmos.esa.int/web/gaia/table-2-with-ascii>

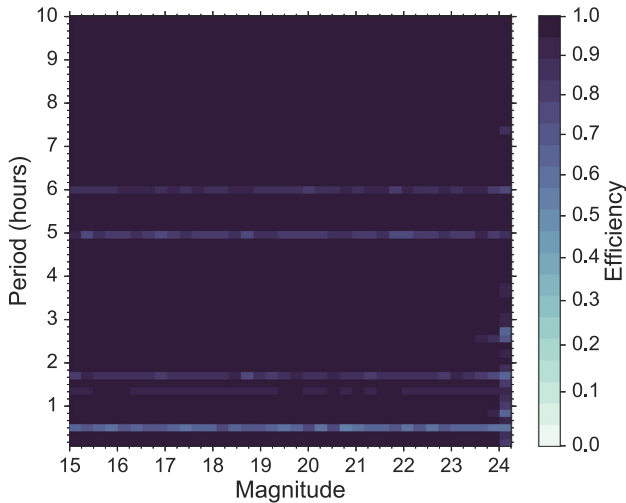


Figure 5. Detection efficiency of the LSST computed for test binary system with $m_1 = 0.53 M_\odot$, $m_2 = 0.35 M_\odot$, $R_2 = 0.017 R_\odot$, $R_1 = 0.8 R_2$, $d = 1$ kpc and $i = \pi/2$. The time step is 10 min and the magnitude step is 0.25. The colour indicates the instrument efficiency from 0 to 1.

3.3 Results

For each binary in our simulated population, we compute 100 light curve realizations by randomizing over the initial orbital phase. We define the probability of detection as the fraction of times the light curve was positively detected over the total number of light-curve realizations. The following results pertain the fraction of the total Galactic DWD population that is (1) above the photometric limit of the instrument, (2) eclipsing given the orientation with respect to the detector (i.e. such that $\cos i \leq (R_1 + R_2)/a$) and (3) in a sky position covered by the survey. In the reminder, we call this population ‘*Gaia*/LSST input population’. Note that the input population represents the maximum detectable sample for a given survey.

We find that 190 (250) binaries have a non-zero probability⁴ to be detected by *Gaia* in the $\alpha\alpha$ ($\gamma\alpha$) scenario in 5-yr mission lifetime. This represents ~ 50 per cent of the *Gaia* input population in both formation scenarios. Such detection percentage is due to the sparse *Gaia* sampling that spread over the 5-yr mission time makes it difficult to detect systems with very narrow eclipses (see Section 3.2). The average number of detected binaries weighed by the detection probability is 30 for the $\alpha\alpha$ and 50 for the $\gamma\alpha$ CE model, respectively. Essentially, *Gaia* will be sensitive to eclipsing binaries with orbital periods less than a few hours (50 per cent of these have periods < 1.6 h, see Fig. 6) up to the maximum of a few days. The most distant binary detected by *Gaia* is at $d = 3.5$ kpc. In addition, we find that a possible extension of the *Gaia* mission up to 10 yr (Gaia Collaboration et al. 2016, section 5.3.2) will double the average number of detections compared to the nominal 5-yr mission lifetime. Incidentally, when we use a random sampling of the orbital phase, instead of using detailed *Gaia* cadence, we obtain twice as many detections.

Compared to *Gaia*, the ability of the LSST to see much fainter sources gives an order of magnitude more eclipsing binaries: 1100 (1460) DWDs have a non-zero probability of being detected. These detections represent ~ 65 per cent of the LSST input population (for

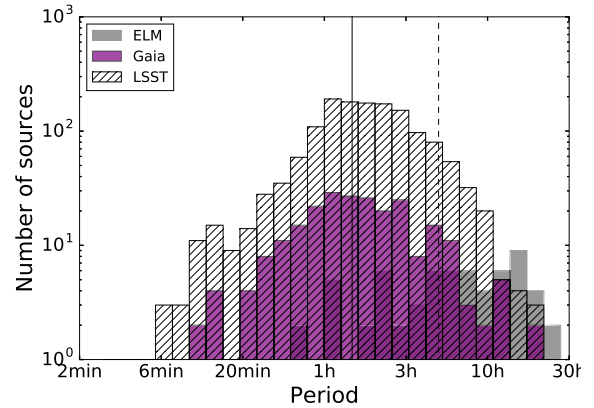


Figure 6. Number of detected sources as a function of the orbital period for the $\gamma\alpha$ formation scenario. The purple and hatched histograms represent, respectively, *Gaia* and LSST detections. The grey histogram shows binaries detected by the ELM survey taken from Gianninas et al. (2015). The black continuous line represents the median of the detected periods in our simulation and dashed line marks the limit of the LISA band.

both formation scenarios). The average number of detected binaries weighed by the probability for the LSST is 850 (1167) DWDs for the $\alpha\alpha$ ($\gamma\alpha$) scenario. The maximum distance in the LSST-detected sample is ~ 10 kpc.

Notably, half of the population detected by both instruments has periods shorter than 1.5 h as shown in Fig. 6. This substantial subsample has orbital frequencies, $f = 1/P$, larger than 0.1 mHz, and thus is potentially detectable through GW radiation in the LISA band (see Section 4). Both *Gaia* and LSST will enlarge the number of very short-period binaries, as the mean period of *Gaia* and LSST detections peaks around 1.5 h, while the mean period of the ELM binaries is 7.4 h (Gianninas et al. 2015).

In Fig. 7, we show the distribution of DWDs weighed by the detection probability in different 2D parameter spaces: the magnitude–period distribution⁵ (top panels), magnitude–Galactic latitude (middle panels) and longitude (bottom panels) distributions, where colours trace the detection probability. The inserts in Fig. 7 represent the respective distributions of all sources with non-zero probability of detection. Despite the fact that *Gaia* is more efficient at brighter magnitudes (Fig. 4), one can see that the majority of the detected population is faint ($G < 18$) and has periods less than a few hours ($P < 3$ h). The former result reflects the magnitude distribution of the input population that peaks around the faint end of the *Gaia* visibility range and the latter is a consequence of our detection criterion as discussed in Section 3.1. Comparing the two upper panels in Fig. 7, it is evident that the LSST with its deeper photometric limit has access to a much larger fraction of the total population. In particular, while *Gaia* operates in the same magnitude range of the ELM ground-based optical survey, the LSST will extend the sample of known DWDs to lower magnitudes. However, the follow-up spectroscopy of such a faint sources will be a challenge even for upcoming facilities.

In the middle and lower panels of Fig. 7, we represent the spatial distribution of *Gaia* and LSST detections. Because of its

⁴ A non-zero probability according to our definition means at least one detection out of 100 (i.e. ≥ 0.01).

⁵ Note that we show only a part of the magnitude–period parameter space, where the majority of the detected population is located, while the whole range of detected periods extends up to a few days for both instruments, where the detections are sparsely distributed.

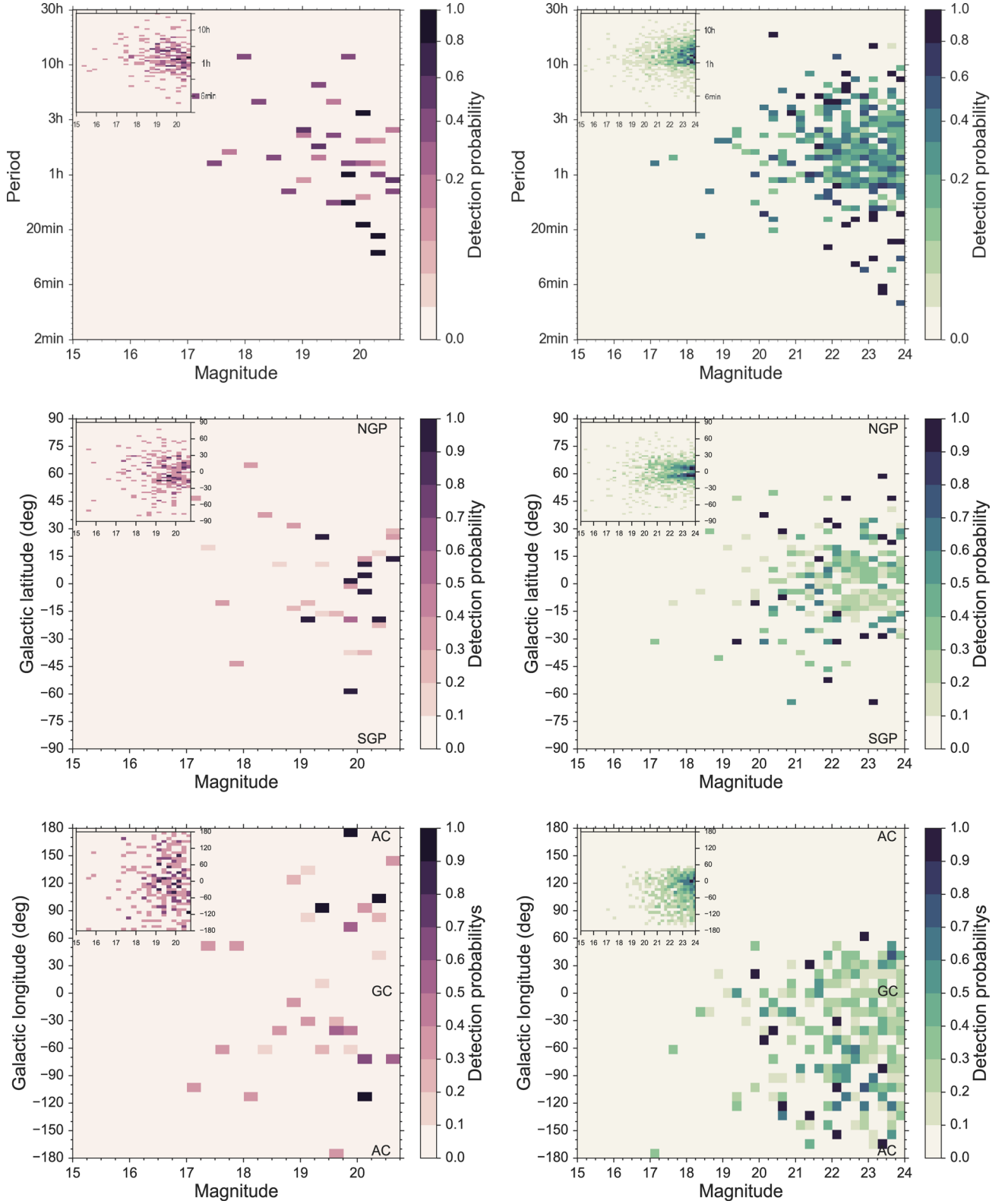


Figure 7. Probability diagrams for the number of detections in different 2D parameter spaces: left-hand panels for *Gaia*, right-hand panels for LSST. We show all the systems formed via the $\gamma\alpha$ scenario weighed by the probability of being detected. The respective inserts represent the distribution of all the systems with a non-zero detection probability. The colour indicates the detection probability: purple palette for *Gaia* and green palette for LSST. NGP and SGP indicate the North and the South Galactic poles, GC and AC indicate Galactic Centre and Galactic anti-centre.

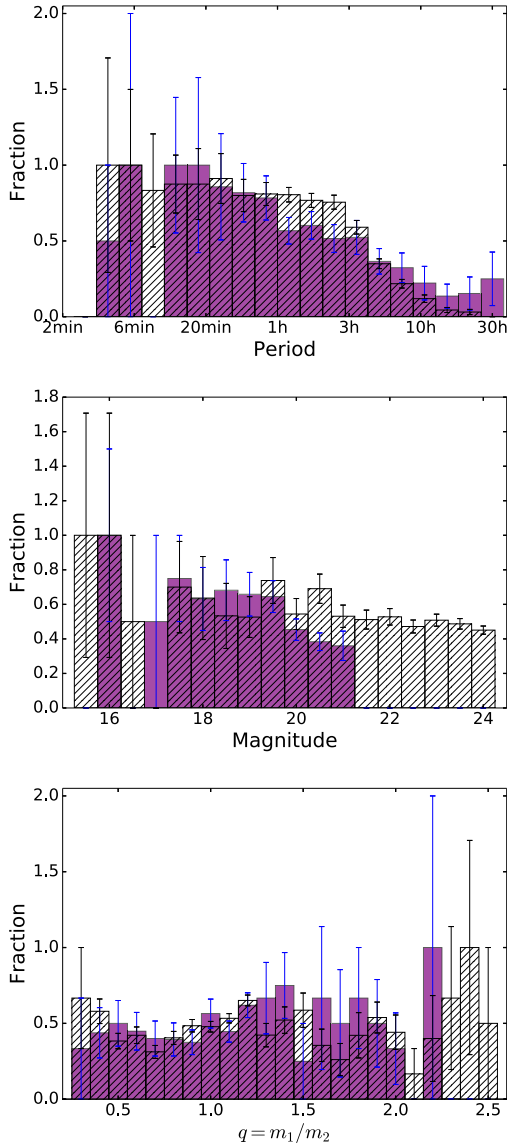


Figure 8. Number ratio of detected sources over the total input binaries per bin for the $\gamma\alpha$ formation scenario. From top to bottom, we show the detection fraction as a function of period, magnitude and mass fraction q . The purple histogram shows *Gaia* detections and hatched histogram represents LSST detections. The error bars (in blue for *Gaia* and in black for the LSST) represent Poissonian errors.

photometric limit, *Gaia* will see only the closest sources ($d_{\max} = 3.5$ kpc \ll radius of Galactic disc); therefore, the distribution in longitude is featureless. On the other hand, one can start to see the distribution of DWD around the Galactic plane (insert middle left panel), since 3.5 kpc is comparable with the vertical extension of the Galactic disc. The distribution of DWDs in the Galaxy will become potentially visible with the LSST. The concentration of detected binaries towards the Galactic plane represents the Bulge of the Galaxy with its characteristic gap around 0° Galactic latitude due to extinction in the disc (insert middle right panel). The location of the LSST in the Southern hemisphere is reflected in the lack of sources for Galactic longitudes greater than 60° in Fig. 7 (bottom right panel).

In Fig. 8, we show the fractions of *Gaia* (purple histogram) and LSST (hatched histogram) detections formed via the $\gamma\alpha$ sce-

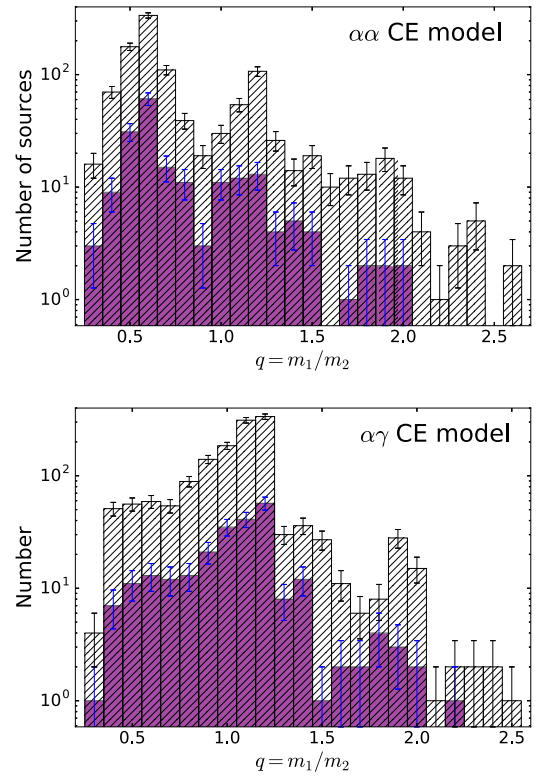


Figure 9. Number of detected sources as a function of binary mass ratio $q = m_1/m_2$ for the two different CE scenarios. The error bars represent Poissonian errors. The colour coding is the same as in Fig. 8.

nario as a function of orbital period, magnitude and binary mass fraction $q = m_1/m_2$. These fractions are defined as a number of detected sources over the number of binaries of the input population per bin. For both instruments, the fraction of detections drops for increasing orbital periods (top panel). Note, however, that the fraction of long period binaries ($P > 24$ h) is higher for *Gaia* (>0.2) due to a non-uniform sampling of the light curves. The middle panel reflects the average detection fraction of the instruments, with no clear preference in magnitude. Both instruments detect high fraction of binaries with $q > 1$ (bottom panel), i.e. systems with more massive primaries. By definition, the primary is the brightest WD (and consequently the biggest) of the pair, so a wider range of inclination angles is allowed for these systems in order to be detected as eclipsing sources, and thus they are more likely to be detected. In our simulation, these systems are typically formed via stable mass transfer. However, taking into account the size of the error bars, the distribution looks consistent with a flat distribution.

Fig. 9 illustrates the number of detected sources as a function of the mass ratio: top panel for the $\alpha\alpha$ and bottom panel for the $\gamma\alpha$ CE model. The two distributions are different: the population formed by the $\alpha\alpha$ model shows a prominent peak around $q \sim 0.5$, while the population formed with $\gamma\alpha$ peaks at $q \sim 1$. Despite the $\gamma\alpha$ CE prescription being designed to match the observed DWD binaries (Nelemans et al. 2000; Nelemans & Tout 2005), the number of currently known sources is too low to prefer it with respect to the $\alpha\alpha$ CE model. However, Fig. 9 shows that the *Gaia* sample has the potential to shed light on the nature of the CE phase and physical process that triggers it in DWD progenitor systems, as one can already see the difference between the two models by comparing the purple histograms.

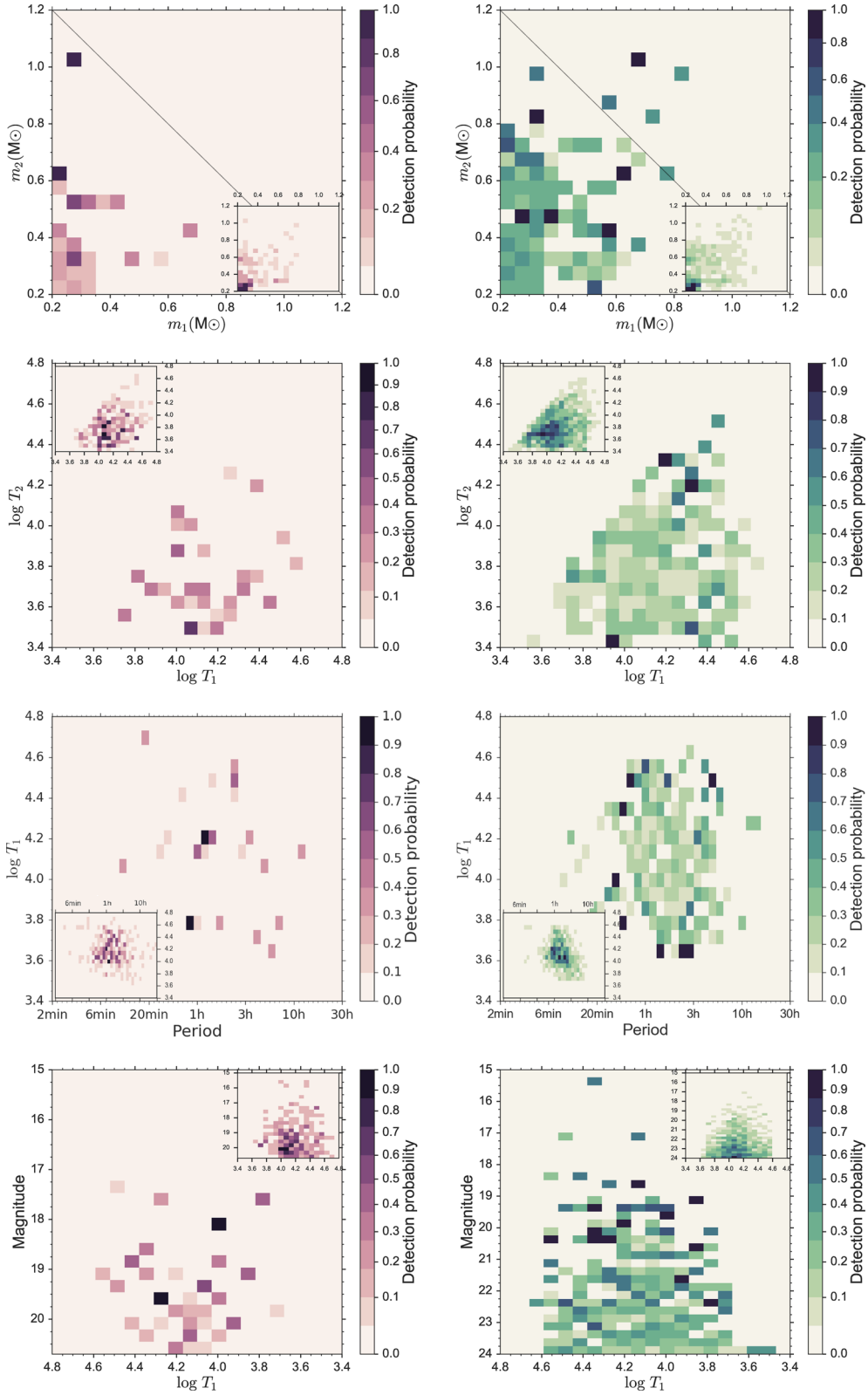


Figure 10. Probability diagrams for the number of *Gaia* and LSST detections as a function of binary parameters. We show all the systems formed via the $\gamma\alpha$ scenario weighed by the probability of being detected. The respective inserts represent the distribution of all the systems with a non-zero detection probability. The colour indicates the number of detected sources: purple palette for *Gaia* and green palette for the LSST. The black solid line (upper panels) represents the Chandrasekhar limiting mass.

In Fig. 10, we illustrate some of the properties of *Gaia* and LSST detections formed by the $\gamma\alpha$ scenario in different 2D parameter spaces where each source is weighed by the detection probability; the inserts represent the respective distributions of the sources with a non-zero probability of being detected. The detected population will consist of binaries with secondaries typically more massive than primaries. The majority of known DWDs were discovered by ELM survey, designed to search for extremely low mass primaries, thus new eclipsing binaries detected by *Gaia* and LSST will extend this parameter space to binaries with more massive primaries. Note that LSST has potential to detect systems with $m_1 + m_2 >$ Chandrasekhar mass limit, providing some SN Ia progenitor candidates. Moreover, the detected population will have primaries hotter than secondaries; therefore, it will be difficult to determine directly the properties of the secondaries. For completeness in the bottom panels of Fig. 10, we represent the distribution of the detected sources in period–temperature and temperature–magnitude space, useful for planning of the spectroscopic followup of these sources.

4 GW DETECTION

In this section, we focus our attention on DWDs as GW sources. First, we recall some basic formulae for the estimation of the GW signal. To simulate the LISA instrument response, in this paper, we adopt the frequency-based method of Cornish & Larson (2003, see also Cutler 1998; Cornish & Rubbo 2003). Then, we estimate the signal-to-noise ratio (SNR) of currently observed DWD binaries to verify our procedure. The following step is to calculate the SNR for all synthetic binaries to identify those with the highest SNR. Finally, we compare our result with previous works (Nelemans et al. 2004; Ruiter et al. 2010; Nissanke et al. 2012), based on a different Galactic model populations.

LISA is a space-based GW interferometer, conceived as a set of three spacecrafts in an equilateral triangle constellation of a few million kilometres per side. Such spacecraft separation sets the sensitivity range of the instrument from about 0.1–100 mHz and will allow the detection of Galactic and extra-Galactic sources, among which thousands will be DWD binaries (Amaro-Seoane et al. 2017). The detector’s centre of mass will follow a circular heliocentric trajectory, trailing 22° behind the Earth and maintaining a 60° inclination between the plane of the detector and the ecliptic plane. As the reference LISA configuration in this work, we adopt the LISA Mission Concept recently submitted as a response to the ESA call for L3 missions (hereafter ESACall v1.1). The ESACall v1.1 is a three-arm configuration⁶ with 2.5×10^6 km arm length instead of 5×10^6 km arm length as in the original LISA project (see e.g. Prince et al. 2007). The sensitivity of the ESACall v1.1 configuration is based on the latest results from the LISA Pathfinder mission (Armano et al. 2016), a precursor mission designed to test the technologies needed for the laser interferometry in space. It is represented in Fig. 11 (Amaro-Seoane et al. 2017).

As pointed out by several authors, at frequencies below a few mHz the expected number of Galactic binaries per frequency bin ($\Delta f = 1/T_{\text{obs}}$, where T_{obs} is the total observation time) is so large that these binaries will form an unresolvable foreground signal in the detector (e.g. Prince et al. 2007; Ruiter et al. 2010; Amaro-Seoane et al. 2012). Fig. 11 illustrates the foreground level from Galactic binaries and its evolution with time from 0.5 to 10 yr of observation

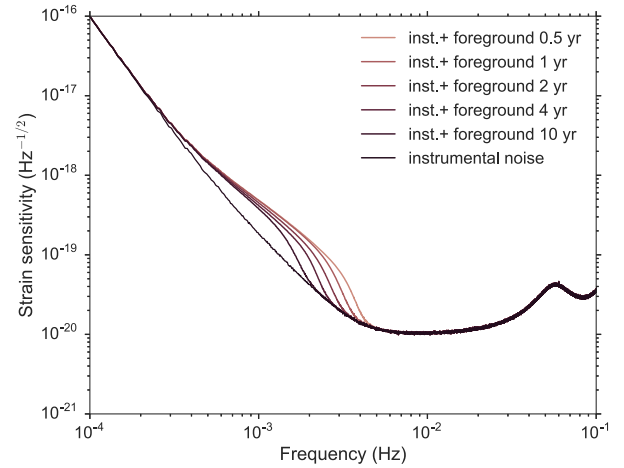


Figure 11. LISA ESACall v1.1 sky-averaged sensitivity due to the instrumental noise only and due to the instrumental noise plus Galactic foreground from DWD binaries after 6 months, 1, 2, 4 and 10 yr of observations (Amaro-Seoane et al. 2017).

computed by using our model population (Amaro-Seoane et al. 2017).

4.1 GW signal from DWDs

The great majority of Galactic DWD binaries can be well described using Newtonian dynamics of circular orbits, under the assumption that the binary can be represented by two point masses in orbit (e.g. van den Broek et al. 2012). The GWs they produce can be computed using the quadrupole approximation (see e.g. Landau & Lifshitz 1962; Peters & Mathews 1963). Considering that the time-scale on which DWDs typically evolve ($> \text{Myr}$) is much greater than the lifetime of the LISA mission ($\sim \text{yr}$), they can be treated as monochromatic sources emitting at the frequency $f_s = 2/P$. In this approximation, the GW signal emitted by a binary is given by a combination of the two polarizations:

$$h_+(t) = \frac{2(G\mathcal{M})^{5/3}(\pi f_s)^{2/3}}{c^4 d} (1 + \cos^2 i) \cos 2\Phi(t), \quad (9)$$

$$h_\times(t) = -\frac{4(G\mathcal{M})^{5/3}(\pi f_s)^{2/3}}{c^4 d} \cos i \sin 2\Phi(t), \quad (10)$$

where $\mathcal{M} = (m_1 m_2)^{3/5} (m_1 + m_2)^{-1/5}$ is the chirp mass of the system and $\Phi(t) = \Phi_0 + \pi f_s t$ is the orbital phase. In the low-frequency limit ($f_s \ll c/2\pi L \sim 20$ mHz, where $L = 2.5$ Mkm is the detector’s arm length), the GW signal as measured by the detector can be expressed as

$$h(t) = F_+ h_+(t) + F_\times h_\times(t), \quad (11)$$

where F_+ and F_\times are the detector pattern functions that encode the dependence of the waveform on the source location in the sky and orientation with respect to the detector and configuration (see equations 9–11 of Cornish & Larson 2003, for specific expression of these functions). For a monochromatic periodic source, the SNR can be written as (Maggiore 2008, equation 7.129):

$$\left(\frac{S}{N}\right)^2 = 4 \int_0^\infty df \frac{|\tilde{h}(f)|^2}{S_n(f)} = \frac{\mathcal{A}^2 T_{\text{obs}}}{S_n(f_s)}, \quad (12)$$

⁶ Note that each arm corresponds to two laser links between spacecrafts, so that a three-arm detector consists of six links in total.

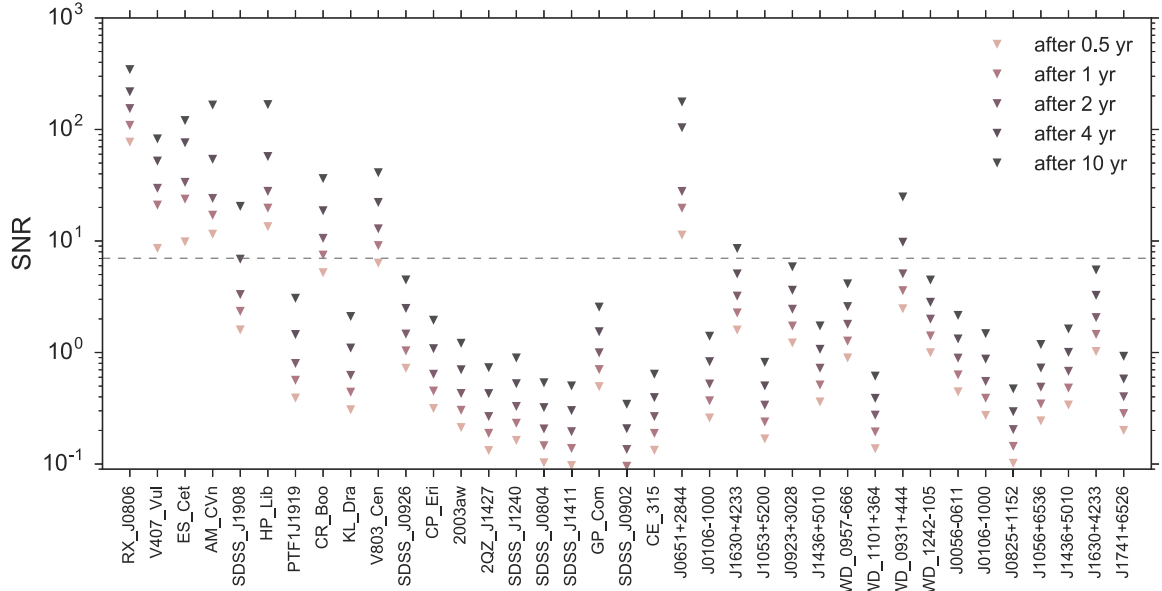


Figure 12. The SNR evolution with time for a sample of LISA verification binaries. The dashed horizontal line corresponds to SNR = 7.

Table 3. Total number of individually resolved DWDs with SNR > 7 for the LISA ESACallv1.1 mission configuration.

CE model	6 m	1 yr	2 yr	4 yr	10 yr
$\alpha\alpha$	6185	9808	16 360	24 482	44 349
$\gamma\alpha$	7125	11 385	18 330	25 754	52 045

where $\tilde{h}(f)$ is the Fourier transform of $h(t)$, $S_n(f_s)$ is the noise spectral density of the instrument at f_s (Fig. 11) and

$$\mathcal{A} = [h_+^2 F_+^2(t) + h_\times^2 F_\times^2(t)]^{1/2}. \quad (13)$$

Note that in equation (12), we substitute the orbit averaged value of \mathcal{A} computed following equations (42–44) of Cornish & Larson (2003).

4.2 Results

To test our method, we consider the sample of the so-called verification binaries. These are well-known ultra-compact binaries (mostly detached DWDs and AM CVns) that are expected to be bright in the LISA band. Consequently, they represent guaranteed sources for the mission. Some of these binaries will be detected in a short period after the beginning of the mission (\sim few months), and thus can be used to verify the performance of the instrument (e.g. Stroeer & Vecchio 2006). Binary parameters and SNR values for 1-yr mission lifetime of the LISA verification binaries are reported in table B1. We find 8 of the 57 verification binaries with SNR > 7 within the first year of observation and 10 within the nominal mission lifetime of 4 yr. These results are in agreement with the full-time domain LISA simulation (A. Petiteau private communication, see also Amaro-Seoane et al. 2017). Fig. 12 illustrates how the SNR grows progressively with mission duration.

We compute the total number of resolved binaries in our model population. Parameters that are not provided directly by our population synthesis code (e.g. the polarization angle and the initial orbital phase) are randomized assuming uniform distribution over the interval of their definition. The result for the two formation scenarios and different mission durations are reported in Table 3. The

Table 4. Summary table for the number of detections with *Gaia*, LSST and LISA. We reported results for the nominal mission lifetime of 5 yr for *Gaia*, 10 yr for the LSST and 4 yr for LISA.

	<i>Gaia</i>	LSST	LISA
(a) $\alpha\alpha$ CE model			
<i>Gaia</i>	189	93	13
LSST	93	1100	50
LISA	13	50	24 508
(b) $\gamma\alpha$ CE model			
<i>Gaia</i>	246	155	25
LSST	155	1457	73
LISA	25	73	25 735

numbers of individually resolved DWDs for the LISA ESACallv1.1 configuration with SNR > 7 are ~ 10 – 11×10^3 for 1 yr and 24.5 – 25.8×10^3 for 4 yr of mission. These results are compatible with those obtained by the Gravitational Observatory Advisory Team (GOAT),⁷ Shah, van der Sluys & Nelemans (2012) and Nissanke et al. (2012), based on Galactic population from Nelemans et al. (2004), and with Ruiter et al. (2010) based on a different population synthesis code, when considering different mission lifetime, detector geometry and SNR threshold.

In Fig. 13, we show some of the properties of LISA detections predicted by the $\gamma\alpha$ CE model. From comparison between Fig. 13 and Fig. 7, it is evident that LISA will see binaries that are non-accessible to EM detectors, virtually down to magnitude 70. LISA detections will have periods ranging between 2 min and 2 h and chirp masses up to $1 M_\odot$. Remarkably, unaffected by extinction LISA will see binaries throughout the Galaxy up to distances comparable with the extension of the Galactic disc. Fig. 13 shows that the most of the detections come from Galactic bulge (i.e. at Galactocentric distance close to 0). (Fig. 13 bottom panels). In particular, LISA

⁷ <http://sci.esa.int/jump.cfm?oid=57910>

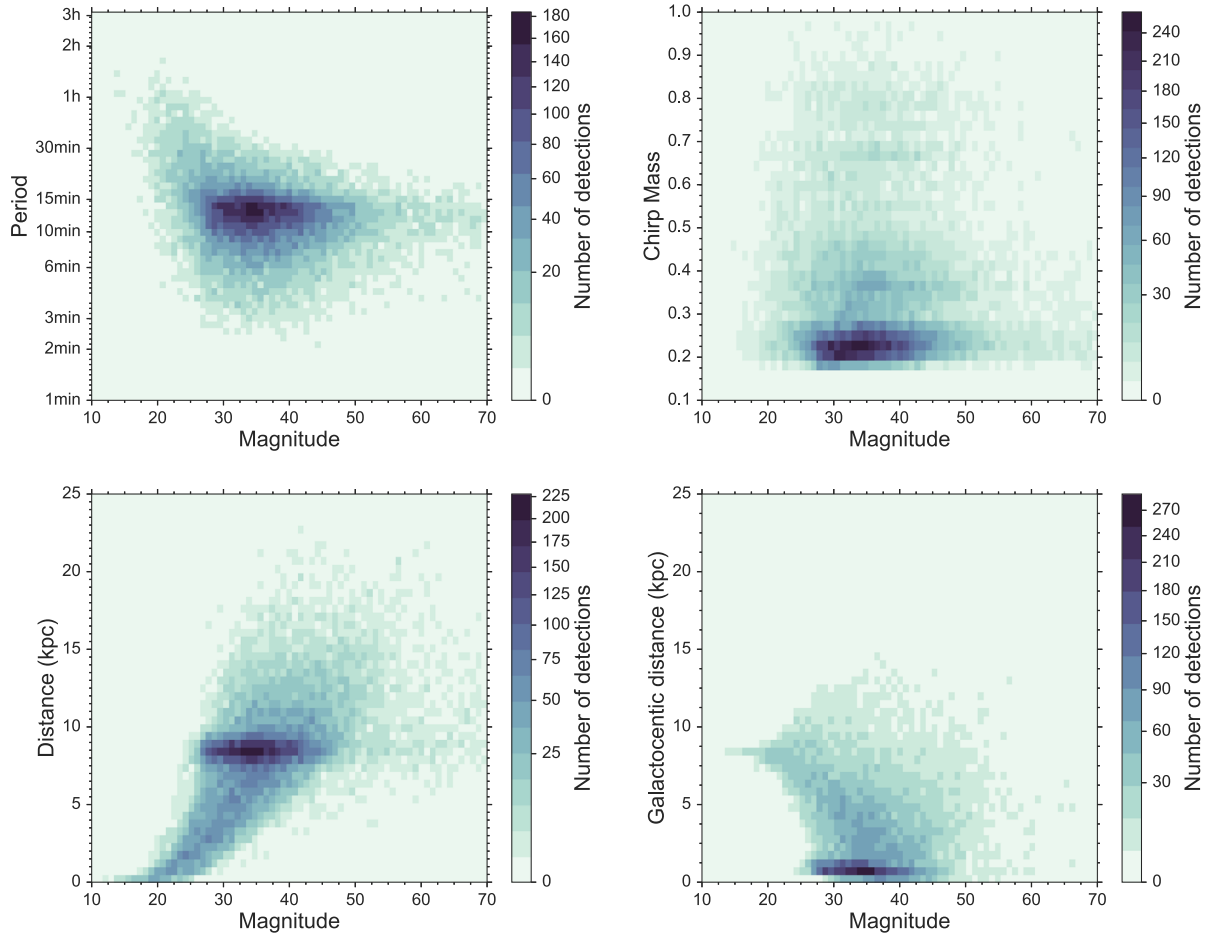


Figure 13. 2D histograms of the number of LISA detections with $\text{SNR} > 7$. The colour indicates the number of detected sources.

will detect DWDs even beyond the Galactic centre that is impossible with optical facilities.

5 THE COMBINED EM AND GW SAMPLE

In the two previous sections, we showed that the expected number of DWD detections through EM and GW radiation within next two decades is significant. So far GW studies focused on currently known Galactic binaries or on the future EM follow-up of these sources, ignoring the fact that revolutionary optical surveys such as *Gaia* and the LSST will be available between now and the LISA launch. In this section, we want to estimate how many DWDs detected by *Gaia* and LSST will be bright enough in GWs to be detected by the LISA.

Starting from the *Gaia* and LSST samples (Section 3), we compute the SNR for the LISA ESACallv1.1 configuration and 4 yr mission lifetime, and we select those with $\text{SNR} > 7$ (see Table 4). We find 13 and 25 combined *Gaia* and LISA detections, respectively, for the $\alpha\alpha$ and $\gamma\alpha$ CE models. Combined LSST and LISA samples are 3–4 times bigger: 50 in the $\alpha\alpha$ formation scenario and 73 for in $\gamma\alpha$ scenario. This result shows that before the LISA launch, we will have at least twice as many guaranteed LISA detections with $\text{SNR} > 7$. The period of the combined detections will range from a few minutes to 1 h and will be on average (as for currently known LISA verification binaries) around 15 min (see Fig. 14). As for the sample of known verification binaries (Table A1), the mass of the primary, secondary and consequently the chirp mass of these bina-

ries is not expected to exceed $1 M_{\odot}$. Verification binaries provided by *Gaia* are not expected to be found at distances larger than the already known ones, while the LSST will double the maximum distance because of its deeper photometric limit (Fig. 14).

Several authors have already pointed out that for those sources that could be detected in both EM and GW waves much more information can be gained compare to either EM or GW can provide alone (see e.g. Marsh 2011; Shah et al. 2012; Shah & Nelemans 2014). Light curves allow the measurement of the orbital period, the inclination angle and the scaled radii of the binary components (R_1/a and R_2/a), that, in turn, can be used to determine the binary mass ratio from the mass–radius relationship. This information combined with the chirp mass determined from the GW data, in principle, permits the estimation of the individual binary component masses. For monochromatic sources, like the majority of DWD binaries, GW data will provide the measurement of the chirp mass in combination with distance (see the dependence on \mathcal{M} and d in equations 9 and 10). Thus, parallax measurements by *Gaia* and LSST will be crucial to determine the distances and to break this degeneracy. The measure of the binary frequency evolution (\dot{f} , that is not likely from GW data for all DWDs) can be equivalently determined from eclipse timing (Shah & Nelemans 2014). Furthermore, the EM observations can be also used to constrain GW observables and to improve their accuracy. In fact, there are several correlations between the GW and EM observable quantities, e.g. between GW amplitude and binary inclination, ecliptic latitude and longitude. For example, an a priori knowledge of the source sky position and inclination can give an

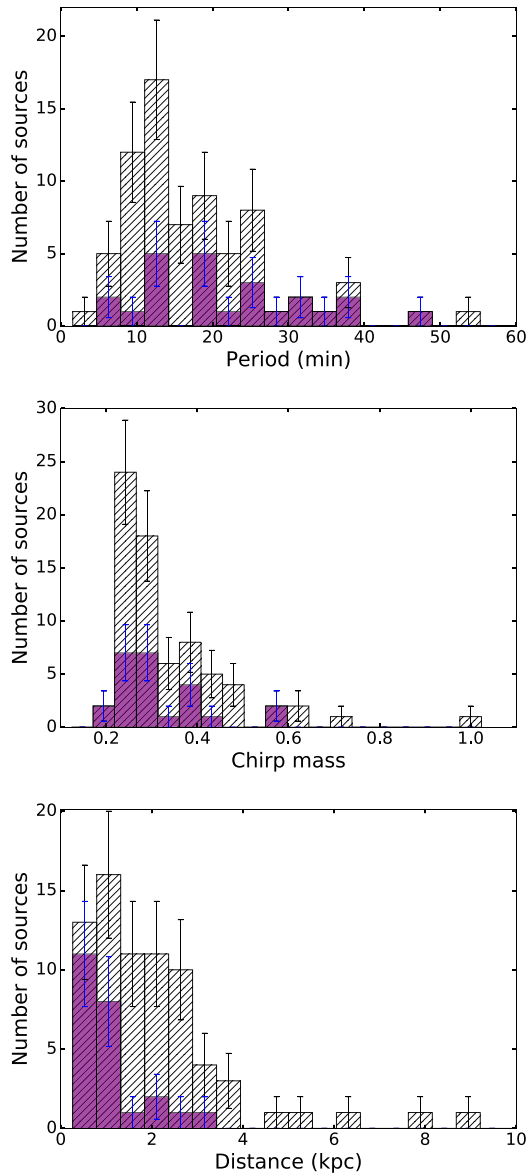


Figure 14. Number of combined EM and GW detections as a function of the chirp mass, binary orbital period and distance from the Sun. The purple histogram represents *Gaia*–*LISA* and hatched histogram represents *LSST*–*LISA* combined detections. The error bars represent Poissonian errors.

improvement on the measurement of GW amplitude up to a factor of 60 (Shah et al. 2013). Vice versa, Shah et al. (2012) showed that small inclination errors from GW data imply that system is eclipsing; consequently, this fact can be used for the EM detection of new eclipsing sources.

6 DISCUSSION AND CONCLUSIONS

In this work, we have computed the expected number of DWD detections by *Gaia* and the *LSST* as eclipsing sources and by the future *LISA* mission as GW sources. As in earlier studies, we relied on population synthesis modelling because of the small number of the known systems. To simulate the Galactic population of DWD binaries, we considered two different prescriptions for the CE phase

($\alpha\alpha$ and $\gamma\alpha$) in order to investigate whether *Gaia*, *LSST* and *LISA* will elucidate on the nature of the CE phase. We find that *Gaia* can provide up to a few hundred of eclipsing detached DWDs, while *LSST* will extend this sample up to almost 2×10^3 sources. Then, we investigated the number of individually resolvable GW sources considering the latest mission concept of the *LISA* detector submitted as a response to the ESA call for L3 missions in 2017. We find that the number of detectable detached DWDs is 25×10^3 for the nominal 4 yr of mission lifetime. Finally, we used the obtained EM samples to estimate how many verification binaries *Gaia* and *LSST* will provide before the *LISA* launch. We find several tens of combined EM and GW detection. These detections will significantly increase the sample of known *LISA* verification binaries by at least factor of 2.

To investigate the sensitivity of our results to assumptions on the initial stellar population, we performed a set of simulations with two different IMFs and with a different mass ratio distribution. We find that the same star formation history but a different choice for the IMF influences mostly the total number of generated DWDs and has a relatively moderate impact on the number of detections. For example, the Miller & Scalo (1979) and the Scalo (1986) IMF, that are steeper than the Kroupa IMF for $M > 1 M_\odot$, produce, respectively, ~ 10 per cent more DWD systems that translates directly in 10 per cent more detections by *Gaia*, *LSST* and *LISA*. On the other hand, the assumption on the mass ratio distribution proves to have a non-negligible impact on our results. In general, a power law $f(q) \propto q^b$ can be used to describe this distribution, where b depends on the stellar population. For intermediate-mass stars, the value of b ranges between 0 and -1 (Duchêne & Kraus 2013). Thus, in addition to our previous simulation (in which we used $b = 0$), we performed a simulation with $b = -1$ to compare the two limiting cases. Such a power law favours unequal mass binaries that need more than a Hubble time to form a DWD. Therefore, we find six times less DWDs than in the original simulation, and, consequently, roughly six times less detections. To verify which of the two mass ratio distributions produce a population that is more compatible with observations, we compare the number of synthetic and observed binaries in the Solar neighbourhood (see unresolved DWD in table 1 of Toonen et al. 2017). We find that the flat mass ratio distribution produces 7 ± 3 DWDs within 20 pc, while a power law with $b = -1$ predicts only 1^{+3}_{-1} . In the observed sample, there is one confirmed isolated DWD and five DWD candidates. The candidates are stars with estimated masses that are too low ($\leq 0.5 M_\odot$) to have evolved as single stars, thus it is highly likely that these are binary stars with undetected companions (see Toonen et al. 2017, and references therein). Because of the large uncertainties in the number of DWDs from both sides: observations and simulations, we cannot place a strong constrain on our synthetic models. We can only conclude that our fiducial model, with the flat mass ratio distribution, is more consistent with the observed numbers within the uncertainties when including the DWD candidates.

The subset of *Gaia* and *LSST* binaries analysed in this work represents guaranteed detections for the *LISA* mission and will provide a powerful tool for probing WD astrophysics and a unique opportunity of multimessenger study for this class of objects. No other GW sources are expected to provide so large number of combined GW and EM detections. We defer to future work for the parameter estimation from EM and GW data for the sample of the combined EM and GW detections and the study of the applicability of these data to the study of the effects of tides in ultra-compact binaries and the kinematics of the Galaxy.

ACKNOWLEDGEMENTS

We would like to acknowledge Antoine Petiteau and Enrico Barausse, who largely contribute to improve our SNR calculation for LISA. We are grateful to Alberto Sesana, Samaya Nissanke, Tom Marsh and Luke T. Maud for useful discussions. We also thank the anonymous referee for valuable comments. This research made use of the *Gaia Observation Forecast Tool*, Astropy, NumPy, Py-Gaia and SciPy PYTHON packages, and matplotlib PYTHON library. This work was supported by NWO WRAP Program, grant NWO 648.003004 APP-GW.

REFERENCES

- Abt H. A., 1983, *ARA&A*, 21, 343
- Amaro-Seoane P. et al., 2012, *Class. Quantum Gravity*, 29, 124016
- Amaro-Seoane P. et al., 2017, preprint ([arXiv:1702.00786](https://arxiv.org/abs/1702.00786))
- Armano M. et al., 2016, *Phys. Rev. Lett.*, 116, 231101
- Badenes C., Mullally F., Thompson S. E., Lupton R. H., 2009, *ApJ*, 707, 971
- Bildsten L., Shen K. J., Weinberg N. N., Nelemans G., 2007, *ApJ*, 662, L95
- Binney J., Tremaine S., 2011, *Galactic Dynamics*, 2nd edn. Princeton Univ. Press, Princeton, NJ
- Boissier S., Prantzos N., 1999, *MNRAS*, 307, 857
- Bours M. C. P. et al., 2014, *MNRAS*, 438, 3399
- Brown W. R., Kilic M., Allende Prieto C., Kenyon S. J., 2010, *ApJ*, 723, 1072
- Carrasco J. M., Catalán S., Jordi C., Tremblay P.-E., Napiwotzki R., Luri X., Robin A. C., Kowalski P. M., 2014, *A&A*, 565, A11
- Cooray A., Farmer A. J., Seto N., 2004, *ApJ*, 601, L47
- Cornish N. J., Larson S. L., 2003, *Phys. Rev. D*, 67, 103001
- Cornish N. J., Rubbo L. J., 2003, *Phys. Rev. D*, 67, 022001
- Cutler C., 1998, *Phys. Rev. D*, 57, 7089
- Dall’Osso S., Rossi E. M., 2014, *MNRAS*, 443, 1057
- De Rosa R. J. et al., 2014, *MNRAS*, 437, 1216
- Debes J. H., Kilic M., Tremblay P.-E., López-Morales M., Anglada-Escudé G., Napiwotzki R., Osip D., Weinberger A., 2015, *AJ*, 149, 176
- Duchêne G., Kraus A., 2013, *ARA&A*, 51, 269
- Evans C. R., Iben I. Jr, Smarr L., 1987, *ApJ*, 323, 129
- Eyer L., Mignard F., 2005, *MNRAS*, 361, 1136
- Eyer L. et al., 2012, in Richards M. T., Hubeny I., eds, *Proc. IAU Symp.* Vol. 282, *From Interacting Binaries to Exoplanets: Essential Modeling Tools*. Cambridge Univ. Press, Cambridge, p. 33
- Eyer L. et al., 2014, *EAS Publ. Ser.*, 67, 75
- Fuller J., Lai D., 2012, *ApJ*, 756, L17
- Gaensicke B. et al., 2015, preprint ([arXiv:1506.02653](https://arxiv.org/abs/1506.02653))
- Gaia Collaboration et al., 2016, *A&A*, 595, A1
- García-Berro E., Badenes C., Aznar-Siguán G., Lorén-Aguilar P., 2017, *MNRAS*, 468, 4815
- Gianninas A., Kilic M., Brown W. R., Canton P., Kenyon S. J., 2015, *ApJ*, 812, 167
- Hallakoun N. et al., 2016, *MNRAS*, 458, 845
- Han Z., 1998, *MNRAS*, 296, 1019
- Heggie D. C., 1975, *MNRAS*, 173, 729
- Hermes J. J., Kilic M., Brown W. R., Montgomery M. H., Winget D. E., 2012, *ApJ*, 749, 42
- Hils D., Bender P. L., Webbink R. F., 1990, *ApJ*, 360, 75
- Holberg J. B., Bergeron P., 2006, *AJ*, 132, 1221
- Iben Icko J., Tutukov A. V., Yungelson L. R., 1997, *ApJ*, 475, 291
- Iben I., Jr, Tutukov A. V., 1984a, *ApJS*, 54, 335
- Iben I., Jr, Tutukov A. V., 1984b, *ApJ*, 284, 719
- Iben I., Jr, Tutukov A. V., Fedorova A. V., 1998, *ApJ*, 503, 344
- Ivanova N. et al., 2013, *A&AR*, 21, 59
- Jonker P. G. et al., 2011, *ApJS*, 194, 18
- Jurić M. et al., 2008, *ApJ*, 673, 864
- Kilic M., Brown W. R., Gianninas A., Hermes J. J., Allende Prieto C., Kenyon S. J., 2014, *MNRAS*, 444, L1
- Kowalski P. M., Saumon D., 2006, *ApJ*, 651, L137
- Kroupa P., Tout C. A., Gilmore G., 1993, *MNRAS*, 262, 545
- Landau L. D., Lifshitz E. M., 1962, *The Classical Theory of Fields*, 2nd edn. Pergamon, London. Available at: <https://cds.cern.ch/record/101809>
- Lipunov V. M., Postnov K. A., 1987, *SvA*, 31, 228
- Littenberg T. B., Larson S. L., Nelemans G., Cornish N. J., 2013, *MNRAS*, 429, 2361
- Longland R., Lorén-Aguilar P., José J., García-Berro E., Althaus L. G., Isern J., 2011, *ApJ*, 737, L34
- Lorén-Aguilar P., Guerrero J., Isern J., Lobo J. A., García-Berro E., 2005, *MNRAS*, 356, 627
- LSST Science Collaboration et al., 2009, preprint ([arXiv:0912.0201](https://arxiv.org/abs/0912.0201))
- Macfarlane S. A., Toma R., Ramsay G., Groot P. J., Woudt P. A., Drew J. E., Barentsen G., Eisloffel J., 2015, *MNRAS*, 454, 507
- McKernan B., Ford K. E. S., 2016, *MNRAS*, 463, 2039
- Maggiore M., 2008, *Gravitational Waves: Theory and Experiments*. Oxford Univ. Press, Oxford. Available at: <https://cds.cern.ch/record/1080850>
- Marsh T. R., 1995, *MNRAS*, 275, L1
- Marsh T. R., 2011, *Class. Quantum Gravity*, 28, 094019
- Marsh T. R., Dhillon V. S., Duck S. R., 1995, *MNRAS*, 275, 828
- Marsh T. R., Nelemans G., Steeghs D., 2004, *MNRAS*, 350, 113
- Maxted P. F. L., Marsh T. R., 1999, *MNRAS*, 307, 122
- Miller G. E., Scalo J. M., 1979, *ApJS*, 41, 513
- Napiwotzki R. et al., 2003, *The Messenger*, 112, 25
- Nelemans G., 2013, in Auger G., Binétruy P., Plagnol E., eds, *ASP Conf. Ser. Vol. 467, 9th LISA Symposium*. Astron. Soc. Pac., San Francisco, p. 27
- Nelemans G., Tout C. A., 2005, *MNRAS*, 356, 753
- Nelemans G., Verbunt F., Yungelson L. R., Portegies Zwart S. F., 2000, *A&A*, 360, 1011
- Nelemans G., Yungelson L. R., Portegies Zwart S. F., Verbunt F., 2001a, *A&A*, 365, 491
- Nelemans G., Yungelson L. R., Portegies Zwart S. F., 2001b, *A&A*, 375, 890
- Nelemans G., Yungelson L. R., Portegies Zwart S. F., 2004, *MNRAS*, 349, 181
- Nissanke S., Vallisneri M., Nelemans G., Prince T. A., 2012, *ApJ*, 758, 131
- Paczynski B., 1976, *Postepy Astron.*, 24, 207
- Perets H. B. et al., 2010, *Nature*, 465, 322
- Perlmutter S. et al., 1999, *ApJ*, 517, 565
- Peters P. C., Mathews J., 1963, *Phys. Rev.*, 131, 435
- Piro A. L., 2011, *ApJ*, 740, L53
- Portegies Zwart S. F., Verbunt F., 1996, *A&A*, 309, 179
- Poveda A., Allen C., Hernández-Alcántara A., 2007, in Hartkopf W. I., Harmanec P., Guinan E. F., eds, *Proc. IAU Symp. Vol. 240, Binary Stars as Critical Tools Tests in Contemporary Astrophysics*. Cambridge Univ. Press, Cambridge, p. 417
- Prince T. A., Binétruy P., Centrella J., Finn L., Hogan C., Nelemans G., Phinney S., 2007, *Bull. Am. Astron. Soc.*, 39, 989
- Prša A., Pepper J., Stassun K. G., 2011, *AJ*, 142, 52
- Raghavan D. et al., 2010, *ApJS*, 190, 1
- Riess A. G. et al., 1998, *AJ*, 116, 1009
- Ruiter A. J., Belczynski K., Benacquista M., Larson S. L., Williams G., 2010, *ApJ*, 717, 1006
- Saffer R. A., Liebert J., Olszewski E. W., 1988, *ApJ*, 334, 947
- Scalo J. M., 1986, *Fund. Cosmic Phys.*, 11, 1
- Schlegel D. J., Finkbeiner D. P., Davis M., 1998, *ApJ*, 500, 525
- Shah S., Nelemans G., 2014, *ApJ*, 791, 76
- Shah S., van der Sluys M., Nelemans G., 2012, *A&A*, 544, A153
- Shah S., Nelemans G., van der Sluys M., 2013, *A&A*, 553, A82
- Sofue Y., Honma M., Omodaka T., 2009, *PASJ*, 61, 227
- Solheim J.-E., 2010, *PASP*, 122, 1133
- Stroeer A., Vecchio A., 2006, *Class. Quantum Gravity*, 23, S809
- Tokovinin A., Mason B. D., Hartkopf W. I., 2014, *AJ*, 147, 123
- Toma R. et al., 2016, *MNRAS*, 463, 1099
- Toonen S., Nelemans G., 2013, *A&A*, 557, A87
- Toonen S., Nelemans G., Portegies Zwart S., 2012, *A&A*, 546, A70

- Toonen S., Hollands M., Gaensicke B. T., Boekholt T., 2017, A&A, 602, A16
- Tremblay P.-E., Bergeron P., Gianninas A., 2011, ApJ, 730, 128
- Tutukov A. V., Yungelson L. R., 1981, Nauchnye Inf., 49, 3
- Tutukov A. V., Yungelson L. R., 1988, Sov. Astron. Lett., 14, 265
- van den Broek D., Nelemans G., Dan M., Rosswog S., 2012, MNRAS, 425, L24
- Webbink R. F., 1984, ApJ, 277, 355

APPENDIX: LIST OF THE LISA VERIFICATION BINARIES

Table A1 shows the sample of currently known DWD and AM CVn systems with expected SNR in GWs > 0.01 , evaluated by using equation (12) for the LISA ESACall v1.1 configuration sensitivity and 1 yr observation time. To roughly estimate SNR values for $T_{\text{obs}} = N_{\text{yr}}$, one can simply rescale the last column by \sqrt{N} .

Table A1. A sample of known interacting (AM CVn stars) and non-interacting (detached DWDs) LISA verification binaries. Amplitudes are given in units of 10^{-23} . To compute the SNR for each binary, we set the initial orbital phase and polarization angle to 0° and the inclination to 60° for cases where it is unknown.

Name	$l_{\text{gal}} (^\circ)$	$b_{\text{gal}} (^\circ)$	P (s)	m_1 (M_\odot)	m_2 (M_\odot)	d (pc)	i ($^\circ$)	f_{GW} (mHz)	\mathcal{A}	SNR
RX J0806 ^a	206.93	23.4	321.529 11	0.55	0.27	5000.0	37.0	6.22	6.43	108.82
V407 Vul ^a	57.73	6.44	569.395	0.6	0.07	2000.0	60.0	3.51	3.32	20.98
ES Cet ^a	168.97	−65.86	621.0	0.6	0.06	1000.0	60.0	3.22	5.4	23.72
AM CVn ^a	140.23	78.94	1028.73	0.71	0.13	600.0	43.0	1.94	15.22	17.03
SDSS J1908+3940 ^a	70.66	13.93	1092.0	0.6	0.05	1000.0	60.0	1.83	3.11	2.34
HP Lib ^a	352.06	32.55	1103.0	0.57	0.06	200.0	30.0	1.81	17.77	19.7
PTF1J1919+4815 ^a	79.59	15.59	1350.0	0.6	0.04	2000.0	60.0	1.48	1.08	0.56
CR Boo ^a	340.96	66.49	1471.0	0.79	0.06	340.0	30.0	1.36	10.82	7.47
KL Dra ^a	91.01	19.2	1500.0	0.6	0.02	1000.0	60.0	1.33	1.02	0.44
V803 Cen ^a	309.37	20.73	1596.0	0.84	0.08	350.0	14.0	1.25	13.75	9.08
SDSS J0926 ^a	187.51	46.01	1699.0	0.85	0.04	460.0	83.0	1.18	5.13	1.03
CP Eri ^a	191.7	−52.91	1701.0	0.6	0.02	700.0	60.0	1.18	1.34	0.45
2003aw ^a	235.13	26.48	2028.0	0.6	0.02	700.0	60.0	0.99	1.19	0.3
2QZ 1427−01 ^a	345.67	37.17	2194.0	0.6	0.015	700.0	60.0	0.91	0.85	0.19
SDSS J1240 ^a	297.57	60.77	2242.0	0.6	0.01	400.0	60.0	0.89	0.98	0.23
SDSS J0804 ^a	205.94	23.37	2670.0	0.6	0.01	400.0	60.0	0.75	0.87	0.15
SDSS J1411 ^a	91.89	63.82	2760.0	0.6	0.01	400.0	60.0	0.72	0.85	0.14
GP Com ^a	323.55	80.3	2794.0	0.6	0.01	80.0	60.0	0.72	4.24	0.7
SDSS J0902 ^a	184.42	41.32	2899.0	0.6	0.01	500.0	60.0	0.69	0.66	0.1
SDSS J1552 ^a	51.31	50.53	3376.3	0.6	0.01	500.0	60.0	0.59	0.6	0.07
CE 315 ^a	309.26	39.25	3906.0	0.6	0.006	77.0	60.0	0.51	2.12	0.19
J0651+2844 ^a	186.93	12.69	765.4	0.55	0.25	1000.0	86.9	2.61	16.84	19.67
J0106−1000 ^a	135.72	−72.47	2346.0	0.43	0.17	2400.0	67.0	0.85	1.95	0.37
J1630+4233 ^a	67.076	43.3603	2390.0	0.31	0.52	830.0	60.0	0.84	11.0	2.26
J1053+5200 ^a	156.4	56.79	3680.0	0.2	0.26	1100.0	60.0	0.54	2.44	0.24
J0923+3028 ^a	195.82	44.78	3884.0	0.279	0.37	228.0	60.0	0.51	20.13	1.73
J1436+5010 ^a	89.01	59.46	3957.0	0.24	0.46	800.0	60.0	0.51	5.91	0.51
WD 0957−666 ^a	287.14	−9.46	5296.81	0.32	0.37	135.0	68.0	0.38	31.07	1.27
J0755+4906 ^a	169.76	30.42	5445.0	0.176	0.81	2620.0	60.0	0.37	1.68	0.08
J0849+0445 ^a	222.7	28.27	6800.0	0.176	0.65	1004.0	60.0	0.29	3.22	0.09
J0022−1014 ^a	99.2997	−71.7538	6902.496	0.21	0.375	1151.0	60.0	0.29	2.15	0.06
J2119−0018 ^a	51.58	−32.54	7497.0	0.74	0.158	2610.0	60.0	0.27	1.15	0.02
J1234−0228 ^a	294.25	60.11	7900.0	0.09	0.23	716.0	60.0	0.25	1.01	0.02
WD 1101+364 ^a	184.48	65.62	12 503.0	0.36	0.31	97.0	25.0	0.16	23.22	0.19
WD 0931+444 ^b	176.08	47.38	1200.0	0.32	0.14	660.0	70.0	1.67	7.41	3.58
WD 1242−105 ^c	300.31	51.98	10 260.0	0.56	0.39	39.0	45.1	0.19	114.75	1.41
J0056−0611 ^d	126.6604	−69.0278	3748.0	0.174	0.46	585.0	60.0	0.53	6.28	0.63
J0106−1000 ^d	135.7244	−72.4861	2345.76	0.191	0.39	2691.0	60.0	0.85	1.79	0.39
J0112+1835 ^d	129.77	−44.0119	12 699.072	0.62	0.16	662.0	60.0	0.16	2.84	0.01
J0345+1748 ^d	171.051	−28.4018	20 306.592	0.76	0.181	166.0	60.0	0.1	10.81	0.01
J0745+1949 ^d	200.4746	20.4396	9711.36	0.1	0.156	270.0	60.0	0.21	1.9	0.02
J0751−0141 ^d	221.4565	12.5761	6912.864	0.97	0.194	1859.0	60.0	0.29	2.52	0.07
J0825+1152 ^d	212.5705	26.1227	5027.616	0.49	0.287	1769.0	60.0	0.4	2.8	0.14
J1053+5200 ^d	156.4021	56.794	3677.184	0.26	0.213	1204.0	60.0	0.54	2.36	0.23
J1054−2121 ^d	269.7458	33.8695	9019.296	0.39	0.168	751.0	60.0	0.22	2.33	0.03
J1056+6536 ^d	140.067	47.5033	3759.264	0.34	0.338	1421.0	60.0	0.53	3.62	0.35
J1108+1512 ^d	234.1026	63.2376	10 635.84	0.42	0.167	698.0	60.0	0.19	2.36	0.02
J1112+1117 ^d	242.321	61.8382	14 902.272	0.14	0.169	257.0	60.0	0.13	2.14	0.01
J1130+3855 ^d	172.9043	69.3762	13 523.328	0.72	0.286	662.0	60.0	0.15	5.2	0.02
J1436+5010 ^d	89.0112	59.4607	3957.12	0.46	0.233	830.0	60.0	0.51	5.55	0.48
J1443+1509 ^d	14.0206	61.3102	16 461.792	0.84	0.181	540.0	60.0	0.12	4.11	0.01

Table A1 – *continued.*

Name	$l_{\text{gal}} (^{\circ})$	$b_{\text{gal}} (^{\circ})$	P (s)	m_1 (M_{\odot})	m_2 (M_{\odot})	d (pc)	i ($^{\circ}$)	f_{GW} (mHz)	\mathcal{A}	SNR
J1630+4233 ^d	67.076	43.3603	2389.824	0.3	0.307	820.0	60.0	0.84	7.06	1.45
J1741+6526 ^d	95.1544	31.7085	5279.904	1.11	0.17	936.0	60.0	0.38	5.82	0.28
J1840+6423 ^d	94.3694	25.424	16 528.32	0.65	0.177	676.0	60.0	0.12	2.66	0.01
J2338–2052 ^d	49.5602	–72.1995	6604.416	0.15	0.263	1295.0	60.0	0.3	1.11	0.03
CSS 41177 ^e	210.129	52.424	8208.0	0.36	0.31	473.0	88.9	0.24	6.3	0.06
J1152+0248 ^f	270.23	61.86	8602.0	0.47	0.41	464.0	89.2	0.23	9.82	0.1

Notes. ^ahttp://www.astro.ru.nl/helemans/dokuwiki/doku.php?id=verification_binaries:intro, ^bKilic et al. (2014), ^cDebes et al. (2015), ^dGianninas et al. (2015), ^eBours et al. (2014), ^fHallakoun et al. (2016).

This paper has been typeset from a \LaTeX file prepared by the author.